

Electronic Wigner-Molecule Polymeric Chains in Elongated Silicon Quantum Dots and Finite-Length Quantum Wires

Arnon Goldberg,^{*} Constantine Yannouleas,[†] and Uzi Landman[‡]
School of Physics, Georgia Institute of Technology, Atlanta, Georgia 30332-0430
(Dated: 03 February 2024)

The spectral properties of electrons confined in a wire-like quasi-one-dimensional (1D) elongated quantum dot (EQD) coupler between silicon qubits, are investigated with a newly developed valley-augmented unrestricted Hartree-Fock (va-UHF) method, generalized to include the valley degree of freedom treated as an isospin, allowing calculations for a large number of electrons. The lower energy symmetry-broken solutions of the self-consistent generalized Pople-Nesbet equations exhibit, for a confinement that has been modeled after an experimentally fabricated one in silicon, formation of Wigner-molecular polymeric (longitudinal) chains, initiating through charge accumulation at the edges of the finite-length quasi-1D wire. An increasing number of parallel zig-zag chains form as the number of electrons loaded into the confinement is increased, with the formation of newly added chains determined by the strength of the transverse harmonic confinement. The broken-symmetry va-UHF solutions, subsequently augmented by the quantum-mechanically required parity-restoration, go beyond the va-UHF single-determinant solution, predicting formation of entangled Wigner-molecular chains whose charge distributions obliterate the zig-zag organization of the broken-symmetry solutions. The symmetry-restored va-UHF methodology enables systematic investigations of multi-electron complex nano-scale confined structures that could be targeted for future imaging microscopy experiments in silicon and other materials (e.g., 1D domain walls in TMD materials), and quantum information utilization.

I. INTRODUCTION

Quantum-dot (QD) qubits are fundamental elements for semiconductor-based solid-state quantum computing architectures [1–3]. One of the central challenging issues in constructing scalable quantum processors is that of quantum chip large-scale integration, allowing transfer of information between computing qubits while preserving information during transfer.

Currently, attention focuses on patterned, gate-controlled elongated quantum dots (EQDs) enabling coherent transfer of spins between relatively distant quantum-dot qubits [4–7], thus reducing the complexity and technical difficulties that accompany short distance multi-dot couplers. To overcome the challenges of designing qubit coupling strategies, recent developments [6, 7] focus on silicon-based nanodevices [1, 2] guided by: (i) the long coherence gained via the use of enriched ²⁸Si substrates, (ii) the successful demonstrations of Si-based high-speed operation and high fidelity spin quantum qubits, and (iii) the vast investment made in the industry and the ensuing infrastructure availability, as well as the scientific experience gained already with Si-based technologies.

Here we aim at gaining fundamental insights about the many-body quantum nature of the electronic states in such patterned, long-distance-coupling EQDs. Such understanding is imperative for enabling theory-guided fabrication and integration of these elements into solid-

state Si-based quantum information devices. Our main finding is that the extended nature of the (wire-like) EQD results in conditions where the inter-electron repulsion energy dominates over the electron quantal kinetic energy. These conditions underlie the emergent formation of pinned Wigner Molecules (WMs), exhibiting a general architecture of parallel chains. Quantum WMs (manifesting sliding [8] or pinned geometrical configurations) have been predicted theoretically (see, e.g., Refs. [9–17]), and subsequently confirmed experimentally in several materials systems (Ga[Al]As single QDs [18, 19], GaAs double QDs [20–22], Si QDs [23, 24], carbon nanotubes [25]), and most recently, in agreement with the latest theoretical predictions [26, 27], in moiré superstructures in transition metal dichalcogenide (TMD) materials [28].

Naturally, one proceeds by formulating the many-body Hamiltonian describing the wire-like EQD, and by numerically solving the corresponding Schrödinger equation. The most accurate method to this effect is exact diagonalization (EXD) through the use of full configuration interaction (FCI) [14, 16, 22, 24, 29, 30], which is limited to systems containing up to about 10 confined electrons, whereas the systems of relevance for qubit couplers are expected to consist of a much larger number of electrons. Accordingly, we employ the unrestricted Hartree-Fock (UHF) [9, 11, 16, 31], which refers to a family of self-consistent field calculation techniques.

The UHF methodology uncovers formation of crystalline-like space-symmetry-broken charge densities (CDs), which are finite-size analogs of the Wigner-crystal chains investigated previously theoretically in the classical limit [32] and in the context of Heisenberg chain modeling [33], as well as investigated experimentally for very long GaAs/AlGaAs wires [34, 35].

^{*} agoldberg36@gatech.edu

[†] Constantine.Yannouleas@physics.gatech.edu

[‡] Uzi.Landman@physics.gatech.edu

A proper quantum mechanical description requires the restoration [11, 16, 36] of the UHF broken symmetries with respect to all the symmetry operations commuting with the system Hamiltonian. Such symmetry restoration is implemented here with respect to the y -parity symmetry about the long x -axis of the EQD. We discovered that the parity-symmetry-restored solutions yield a substantially improved description of the CDs compared to those given by the broken-symmetry UHF solutions. Moreover, this improvement, involving an extension beyond the variational UHF single-determinant ansatz, proves to be most efficient, entailing a rather minimal computational cost for systems involving a relatively large number (dozens) of electrons.

Furthermore, the present implementation of the UHF method requires consideration of the valley degree of freedom which is present in silicon nanostructures, treated here as a pseudospin (along the spin). This requires modifications (employed in this paper; see Sec. III) of the UHF Pople-Nesbet equations [9, 11, 16] formulated originally in quantum chemistry for the case of natural molecules [31]. We will interchangeably refer to our calculations as UHF or valley-augmented UHF (va-UHF).

II. MANY-BODY HAMILTONIAN

We consider a square-like, slightly asymmetric, confining potential along the lateral long axis (the x -axis) of the EQD specified by:

$$U_L(x) = \xi|x/x_0|^9\Theta(-x) + \xi(x/x_0)^{10}\Theta(x), \quad (1)$$

where $\Theta(x)$ is the Heaviside step function, $x_0 = 50$ nm, and $\xi = 0.1$ meV. This confinement corresponds to the

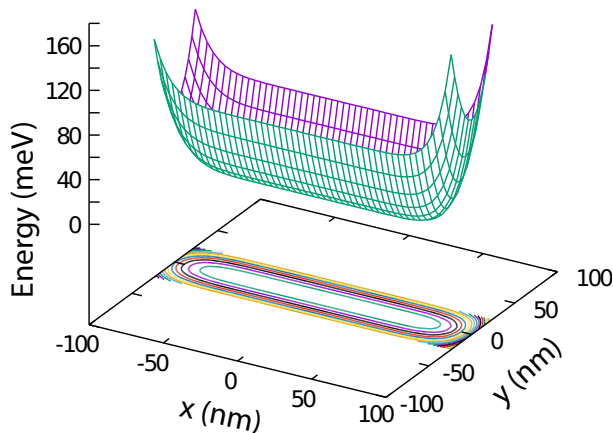


FIG. 1. An illustration of the longboat-Viking-type total confining potential $U(x, y)$ used. The square-type lateral potential, $U_L(x)$, along the x -axis is given by Eq. (1). The transverse harmonic potential, $U_T(y)$, along the y -direction corresponds to $\hbar\omega_y = 10$ meV and to an effective electron mass $m^* = 0.19m_e$ (appropriate for silicon).

EQD (referred to also as jellybean QD) fabricated (including the above-noted slight asymmetry) and investigated in Ref. [6]. The total confinement is given by

$$U(x, y) = U_L(x) + U_T(y), \quad (2)$$

where $U_T(y) = m^*\omega_y^2 y^2/2$ is a harmonic potential along the transverse y -direction; $m^* = 0.19m_e$ is the effective electron mass for Si and $\hbar\omega_y$ the harmonic quantum in the transverse y -direction.

An illustration of $U(x, y)$ is presented in Fig. 1. Furthermore, an illustration of the associated (single-particle) spectrum (with $\hbar\omega_y = 2.5$ meV and $m^* = 0.19m_e$) is plotted in Fig. 2.

The relevant many-body Hamiltonian is given by:

$$H_{\text{MB}} = \sum_{i=1}^N \left(\frac{\mathbf{p}_i^2}{2m^*} + U(\mathbf{r}_i) \right) + \frac{e^2}{\kappa} \sum_{i=1}^{N-1} \sum_{j>i}^N \frac{1}{|\mathbf{r}_i - \mathbf{r}_j|}, \quad (3)$$

where κ is the dielectric constant.

III. THE VALLEY-AUGMENTED UNRESTRICTED HARTREE-FOCK FOR NANOSYSTEMS

Due to strain in Si/SiGe quantum wells and (interfacial) quantum dots (in particular, in heterostructure semiconductors) and higher subband quantization energy in metal-oxide-semiconductor devices, the energies of the (four) in-plane Si valleys are raised, resulting in two remaining degenerate valleys. In this paper, as is the case for the general practice for the Si QDs [37], we consider that the valley degree of freedom (VDOF) consists only of the low-energy two-fold band.

As elaborated in Ref. [24], to characterize and classify the VDOF of the two remaining valleys, we consider in

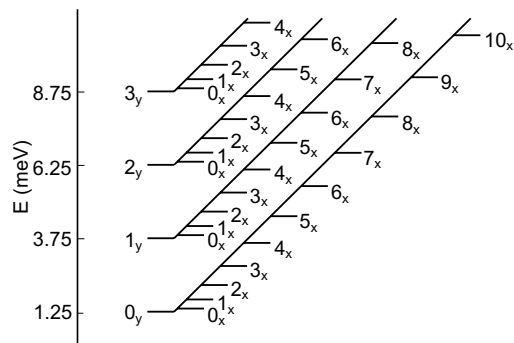


FIG. 2. An illustration of the single-particle spectrum of electrons in the potential, $U(x, y)$, used to model the elongated QD investigated in this paper. For the parameters, see the text. The labels for the single-particle space orbitals are as follows: $n_x \rightarrow$ number of nodes in the x -direction. $n_y \rightarrow$ number of nodes in the y -direction.

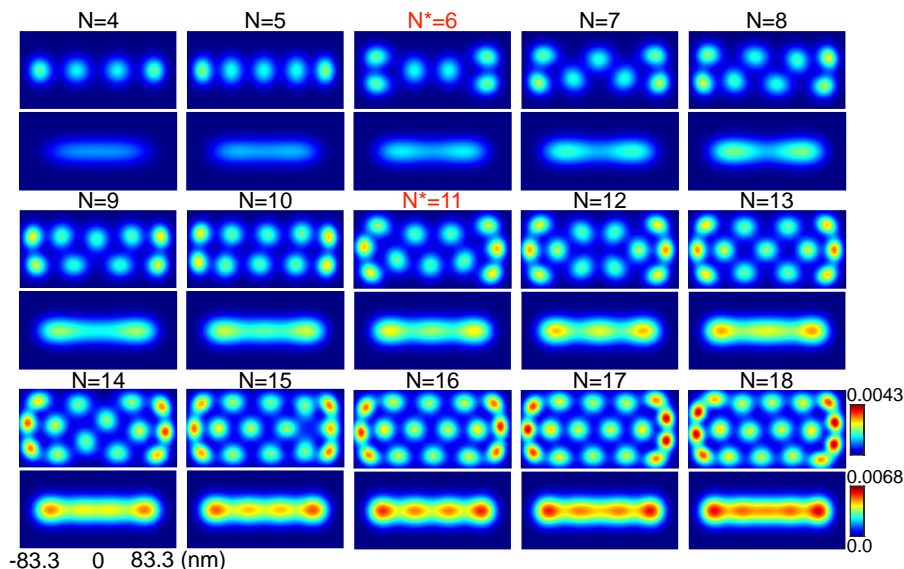


FIG. 3. UHF ground-state charge densities (CDs) for $N = 4 - 18$ electrons in a silicon elongated quantum dot (~ 110 nm long), with a transverse confinement of $\hbar\omega_y = 2.5$ meV. For each N the CD is shown for strongly repelling electrons ($\kappa = 11$) at the top, and the CD for electrons in the non-interacting limit is shown at the bottom. The non-interacting CDs (at maximum occupation per orbital, large $\kappa = 300$, and $\hbar\omega_y = 2.5$ meV) exhibit for all N single-row structures of a delocalized-particle nature, and obey a shell-filling Aufbau rule (following spin and isospin exclusion rules; see text). In contrast, the strongly interacting electrons CDs exhibit a transition from linear Wigner-molecular structures for $N \leq 5$ to a single zig-zag chain at $N^* = 5$ and to a double zig-zag chain at $N^* = 11$, that initiate via charge accumulation occurring at the ends of the EQD. The color bars (bottom right) indicate the charge density scale (in units of $1/\text{nm}^2$). For details, see the text.

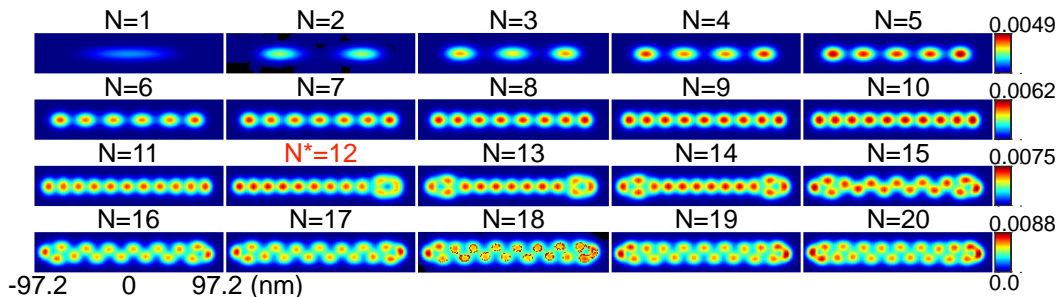


FIG. 4. UHF ground-state CDs for $N = 1 - 20$ electrons for a silicon EQD with a transverse confinement of $\hbar\omega_y = 10$ meV. $\kappa = 11$ appropriate for silicon (strong interaction). The CDs exhibit a transition from one-row Wigner-molecular structures for $N \leq 11$ to a zig-zag chain for $N \geq N^* = 12$ that initiates via charge accumulation occurring at the two ends of the EQD (see $N = 12 - 14$), with the zig-zag pattern fully developed for $N = 15 - 20$. For larger number of electrons a three-row zig-zag chain structure emerges (not shown). The color bars (on the right) indicate the charge-density scale (in units of $1/\text{nm}^2$).

this paper an isospin designation that is constructed in analogy [including the $SU(2)$ algebra generated by the i -multiplied Pauli matrices] with that of the regular spin of the electrons (replacing \hat{S} with \hat{V} when referring to the VDOF). Obviously, in the absence of two-body interactions, the occupation of the single-particle energy states [38] in the QDs would depend on an interplay between the confinement (including an applied magnetic field) and the spin and valley effects. For the case of two-valley degeneracy (considered here) this interplay results in “quadrupling” of the spectrum (four degenerate states for each confinement state, each corresponding to a different spin and valley).

Here, we introduce the va-UHF for solving the many-body problem specified by the Hamiltonian H_{MB} defined in Eq. (3). Accordingly, one introduces a basis set of spatial single-particle orbitals $\varphi_\mu(x, y)$, $\mu = 1, \dots, K$, which are given by the K lowest-energy solutions of the auxiliary single-particle Hamiltonian,

$$H^{\text{core}} = \sum_{i=1}^N \left(\frac{\mathbf{p}_i^2}{2m^*} + U(\mathbf{r}_i) \right). \quad (4)$$

For clarity and convenience, these solutions are sorted in ascending energy.

Subsequently, for the four families of va-UHF *spin-*

isospin-orbitals [39], $\psi_i^{\alpha\zeta}\alpha\zeta$, $\psi_i^{\beta\zeta}\beta\zeta$, $\psi_i^{\alpha\eta}\alpha\eta$, $\psi_i^{\beta\eta}\beta\eta$, where $\alpha(\beta)$ denote up (down) spins, $\zeta(\eta)$ denote up (down) isospins [i.e., electrons in the first (second) valley], one considers the expansions:

$$\begin{aligned}\psi_i^{\alpha\zeta} &= \sum_{\mu=1}^K C_{\mu i}^{\alpha\zeta} \varphi_\mu, \\ \psi_i^{\beta\zeta} &= \sum_{\mu=1}^K C_{\mu i}^{\beta\zeta} \varphi_\mu, \\ \psi_i^{\alpha\eta} &= \sum_{\mu=1}^K C_{\mu i}^{\alpha\eta} \varphi_\mu, \\ \psi_i^{\beta\eta} &= \sum_{\mu=1}^K C_{\mu i}^{\beta\eta} \varphi_\mu, \\ i &= 1, 2, \dots, K.\end{aligned}\tag{5}$$

Then, following similar steps as in Ch. 3.8.2 of Ref. [31], we have derived a generalization of the Pople-Nesbet equations as follows:

$$\begin{aligned}\sum_{\nu} F_{\mu\nu}^{\alpha\zeta} C_{\nu j}^{\alpha\zeta} &= \varepsilon_j^{\alpha\zeta} \sum_{\nu} S_{\mu\nu} C_{\nu j}^{\alpha\zeta}, \\ \sum_{\nu} F_{\mu\nu}^{\beta\zeta} C_{\nu j}^{\beta\zeta} &= \varepsilon_j^{\beta\zeta} \sum_{\nu} S_{\mu\nu} C_{\nu j}^{\beta\zeta}, \\ \sum_{\nu} F_{\mu\nu}^{\alpha\eta} C_{\nu j}^{\alpha\eta} &= \varepsilon_j^{\alpha\eta} \sum_{\nu} S_{\mu\nu} C_{\nu j}^{\alpha\eta}, \\ \sum_{\nu} F_{\mu\nu}^{\beta\eta} C_{\nu j}^{\beta\eta} &= \varepsilon_j^{\beta\eta} \sum_{\nu} S_{\mu\nu} C_{\nu j}^{\beta\eta}, \\ j &= 1, 2, \dots, K.\end{aligned}\tag{6}$$

with the Fock-operator matrices being given by,

$$\begin{aligned}F_{\mu\nu}^{\alpha\zeta} &= H_{\mu\nu}^{\text{core}} + \sum_{\lambda} \sum_{\sigma} P_{\lambda\sigma}^T [(\mu\nu|\sigma\lambda) - P_{\lambda\sigma}^{\alpha\zeta}(\mu\lambda|\sigma\nu)], \\ F_{\mu\nu}^{\beta\zeta} &= H_{\mu\nu}^{\text{core}} + \sum_{\lambda} \sum_{\sigma} P_{\lambda\sigma}^T [(\mu\nu|\sigma\lambda) - P_{\lambda\sigma}^{\beta\zeta}(\mu\lambda|\sigma\nu)], \\ F_{\mu\nu}^{\alpha\eta} &= H_{\mu\nu}^{\text{core}} + \sum_{\lambda} \sum_{\sigma} P_{\lambda\sigma}^T [(\mu\nu|\sigma\lambda) - P_{\lambda\sigma}^{\alpha\eta}(\mu\lambda|\sigma\nu)], \\ F_{\mu\nu}^{\beta\eta} &= H_{\mu\nu}^{\text{core}} + \sum_{\lambda} \sum_{\sigma} P_{\lambda\sigma}^T [(\mu\nu|\sigma\lambda) - P_{\lambda\sigma}^{\beta\eta}(\mu\lambda|\sigma\nu)],\end{aligned}\tag{7}$$

and the $\varepsilon_j^{\alpha\zeta}$, $\varepsilon_j^{\beta\zeta}$, $\varepsilon_j^{\alpha\eta}$, $\varepsilon_j^{\beta\eta}$ being the energies for the spin-isospin va-UHF orbitals. Because the φ_μ 's are eigenfunctions of H^{core} , one has $S_{\mu\nu} = \delta_{\mu\nu}$ for their overlaps. The two-body Coulomb matrix elements are given by

$$(\mu\nu|\sigma\lambda) = \frac{e^2}{\kappa} \int d\mathbf{r}_1 d\mathbf{r}_2 \varphi_\mu^*(\mathbf{r}_1) \varphi_\nu(\mathbf{r}_1) r_{12}^{-1} \varphi_\sigma^*(\mathbf{r}_2) \varphi_\lambda(\mathbf{r}_2),\tag{8}$$

with $r_{12}^{-1} = 1/|\mathbf{r}_1 - \mathbf{r}_2|$.

In Eq. (7), the partial density matrices are given by

$$\begin{aligned}P_{\mu\nu}^{\alpha\zeta} &= \sum_a^{N^{\alpha\zeta}} C_{\mu a}^{\alpha\zeta} (C_{\nu a}^{\alpha\zeta})^*, \quad P_{\mu\nu}^{\beta\zeta} = \sum_a^{N^{\beta\zeta}} C_{\mu a}^{\beta\zeta} (C_{\nu a}^{\beta\zeta})^*, \\ P_{\mu\nu}^{\alpha\eta} &= \sum_a^{N^{\alpha\eta}} C_{\mu a}^{\alpha\eta} (C_{\nu a}^{\alpha\eta})^*, \quad P_{\mu\nu}^{\beta\eta} = \sum_a^{N^{\beta\eta}} C_{\mu a}^{\beta\eta} (C_{\nu a}^{\beta\eta})^*,\end{aligned}\tag{9}$$

the total-density matrix is defined as

$$\mathbf{P}^T = \mathbf{P}^{\alpha\zeta} + \mathbf{P}^{\beta\zeta} + \mathbf{P}^{\alpha\eta} + \mathbf{P}^{\beta\eta},\tag{10}$$

and

$$N^{\alpha\zeta} + N^{\beta\zeta} + N^{\alpha\eta} + N^{\beta\eta} = N.\tag{11}$$

The energy eigenvalues ($\varepsilon_j^{\alpha\zeta}$, $\varepsilon_j^{\beta\zeta}$, $\varepsilon_j^{\alpha\eta}$, $\varepsilon_j^{\beta\eta}$) and expansion coefficients ($C_{\nu j}^{\alpha\zeta}$, $C_{\nu j}^{\beta\zeta}$, $C_{\nu j}^{\alpha\eta}$, $C_{\nu j}^{\beta\eta}$) are obtained via self-consistent solutions of Eqs. (6).

We note that, unlike the valleytronic FCI [24], the va-UHF does not conserve the total spin $\hat{\mathbf{S}}^2$ and total valley $\hat{\mathbf{V}}^2$ quantum numbers; it only conserves their projections S_z and V_z .

IV. VA-UHF CHARGE DENSITIES

For $N = 4 - 18$, fully spin and valley polarized ($S_z = V_z = N/2$), electrons and $\hbar\omega_y = 2.5$ meV, Fig. 3 contrasts the UHF CDs at $\kappa = 11$ (silicon, top rows) to those associated with the non-interacting limit (NIL) (at maximum occupation per orbital, $\kappa = 300$, and $\hbar\omega_y = 2.5$ meV, bottom rows). For all the strongly-interacting-electron cases, the UHF densities exhibit explicit configurations of N well defined humps reflecting formation of pinned WMs, associated with the regime of strong inter-electron correlations. In contrast, the NIL CDs conform to those expected from (Aufbau) shell closures in the $U(x, y)$ confinement, with a fourfold period (due to both the spin and valley) being clearly visible for $N = 5 - 8$ [when the $(1_x, 0_y)$ orbital of the confining potential $U(x, y)$ is sequentially occupied (see also Fig. 6); here (n_x, n_y) denotes the number of nodes in the x - and y -directions].

In Fig. 8 of Appendix A, we demonstrate that the CDs shown in Fig. 3 (see also Fig. 9), calculated for the spin and valley fully polarized ($S_z = V_z = N/2$) electrons, are essentially identical to the CDs for the va-UHF states with minimal spin, S_z , and isospin, V_z , projections (0 for even N or $\pm 1/2$ for odd N). This finding concurs with the magneto-spectroscopy measurements [6] where it has been found that the ‘‘Jellybean’’ quantum dot studied in these experiments lacks visible spin structure for similar electron numbers as those investigated in the present paper.

We recall that the strength of correlations is often expressed via the Wigner parameter [9, 16] $R_W = \mathcal{E}_C/\delta$, defined as the ratio of a typical inter-electron repulsive Coulombic energy, \mathcal{E}_C , over a typical energy gap, δ , in

the single-particle spectrum of $U(x, y)$; naturally, the strong-interaction regime is expected for $R_W > 1$, accompanied by WM formation. For the square-like confinement here, we take \mathcal{E}_C as the two-body matrix element of the Coulomb interaction for two electrons occupying the nodeless lowest $(0_x, 0_y)$ orbital, and for δ we take the difference between the energies of the $(0_x, 0_y)$ and $(1_x, 0_y)$ orbitals. For the EQD investigated here, we have $R_W = 23.04$ for $\kappa = 11$ and $\hbar\omega_y = 2.5$ meV, $R_W = 29.14$ for $\kappa = 11$ and $\hbar\omega_y = 10$ meV (strong interactions, case of the Si QD), and $R_W = 0.84$ for $\kappa = 300$ and $\hbar\omega_y = 2.5$ meV (non-interacting limit).

A prominent feature of the WM configurations is the successive formation with increasing N of complex, polymeric, multiple chain-like arrangements, reminiscent of the classical Wigner-crystalline chains associated with the equilibrium configurations of classical point charges [32] in infinite-length wires. Naturally, the presence of the square-like edges here perturbs the perfect-chain formations of the infinite-length wires by forcing an accumulation of charges at the edges. The well-known zig-zag configuration, however, is visible away from the edges of the EQDs for $N = 7 - 11$ (single zig-zag) and for $N = 14 - 18$ (double zig-zag).

We note that a single row appears for $N = 1 - 5$, whilst a second row starts developing at $N = 7$ with $N = 6$ being a transitional stage. A third row starts developing at $N = 11$, whilst transitional cases towards a fourth row appear at $N = 17$ and $N = 18$, with four electrons accumulating in a line along the y -direction at the edges.

Fig. 4 displays the UHF CDs for fully spin and valley polarized $N = 1 - 20$ electrons for a tighter transverse confinement with $\hbar\omega_y = 10$ meV. These CDs exhibit again organization with Wigner-chain-like features, the main difference from the $\hbar\omega_y = 2.5$ meV case [see Fig. 3] being a delay in the appearance (as a function of N) of the transition regions between the multiple chains. In particular, the single chain transitions to a double zig-zag chain at the region $N = 12 - 14$, with the double chain starting to form from the edges [40], a behavior related to the accumulation of charge at the sharp square-like edges of the confinement along the x -direction. Note that, due to this delay, the third row does not appear in Fig. 4 in the range $N = 1 - 20$; for $\hbar\omega_y = 10$ meV, a third row is expected to develop at larger values of N .

V. RESTORATION OF PARITY ALONG THE TRANSVERSE y -DIRECTION

The broken-symmetry UHF solutions violate a fundamental axiom of quantum mechanics, namely, that the single-particle CDs must preserve the symmetries of the many-body Hamiltonian. Here we take a first step in rectifying this UHF inadequacy by restoring the parity symmetry along the transverse y -direction, which is associated with a symmetric harmonic confinement $U_T(-y) = U_T(y)$; note that the confinement along x was

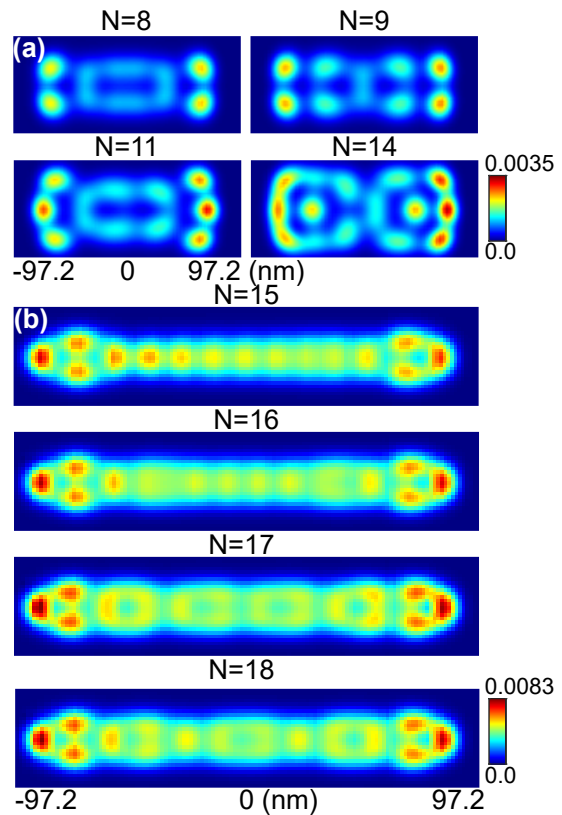


FIG. 5. Parity-restored CDs for a silicon EQD. (a) transverse confinement of $\hbar\omega_y = 2.5$ meV. $N = 8, 9, 11, 14$ fully spin and valley polarized electrons. (b) transverse confinement of $\hbar\omega_y = 10$ meV. $N = 15 - 18$ fully spin and valley polarized electrons. In both cases, $\kappa = 11$ appropriate for silicon (strong interaction). The symmetry-broken UHF CDs, corresponding to the restored ones shown in (a) and (b), are given in Figs. 3 and 4, respectively. Obviously, only symmetry-broken UHF wave-functions undergo symmetry restoration. CDs in units of $1/\text{nm}^2$.

taken to be slightly anisotropic.

To restore the y -parity symmetry, we apply on the UHF Slater determinant (SD), Ψ_{UHF} , the projection operator [16, 36, 41]

$$\hat{\Pi} = \frac{1}{2}(1 + p\hat{P}_y), \quad (12)$$

with $p = \pm 1$. \hat{P}_y is the many-body parity operator, which inverts about the x -axis the y -coordinates for all electrons, namely, $\hat{P}_y = \prod_{i=1}^N \hat{P}_y^{(i)}$.

The charge density associated with the projected wave function $\Psi_{\text{PUHF}} = \hat{\Pi}\Psi_{\text{UHF}}$ is given by

$$\rho_{\text{PUHF}}(\mathbf{r}) = \mathcal{N} \langle \Psi_{\text{UHF}} | \hat{\Pi} \sum_{i=1}^N \delta(\mathbf{r}_i - \mathbf{r}) \hat{\Pi} | \Psi_{\text{UHF}} \rangle, \quad (13)$$

where the factor \mathcal{N} imposes normalization to N . The expansion of the symmetry-restored charge density in Eq. (13) is explicitly displayed in Eq. (C1) of Appendix C.

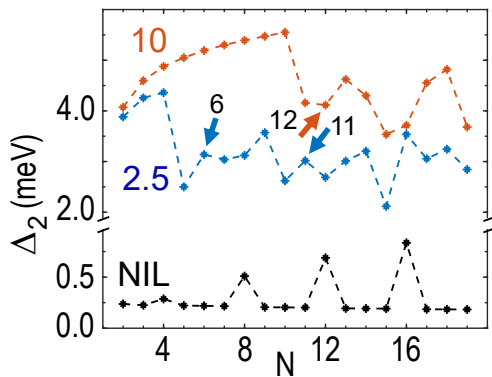


FIG. 6. UHF second energy differences, Δ_2 . The curves associated with $\hbar\omega_y = 2.5$ meV and $\hbar\omega_y = 10$ meV for $\kappa = 11$ (strong interaction), as well as with the non-interacting limit (at maximum occupation per orbital, $\kappa = 300$, and $\hbar\omega_y = 2.5$ meV) are as noted. The arrows denote the transition sizes (N^* 's) between the multiple chains marked in Fig. 3 and Fig. 4.

The projected total energy is given by [16, 36]

$$E_{\text{PUHF}} = \frac{\langle \Psi_{\text{UHF}} | H \hat{\Pi} | \Psi_{\text{UHF}} \rangle}{\langle \Psi_{\text{UHF}} | \hat{\Pi} | \Psi_{\text{UHF}} \rangle}. \quad (14)$$

Eqs. (13) and (14) are calculated using the property $\hat{P}_y^{(z)} Y_n(y) = \varpi_n Y_n(y)$, where $\varpi_n = (-1)^n$, $n = 0, 1, 2, \dots$ and $Y_n(y)$ are the good-parity eigenfunctions of $U_T(y)$.

Several CD results of this parity restoration are displayed in Fig. 5; it is apparent that the zig-zag motif gets obliterated by the parity restoration. Whether a zig-zag or a symmetry-restored CD will be the actual finding in a quasi-1D system may depend in practice on several additional factors, including the presence of impurities, the length of the system, as well as the value of the effective mass. Indeed, the longer the system, the higher the expectation for a broken symmetry CD. Interestingly, because of the much larger mass compared to electrons, the CDs of trapped heavy ions are routinely found experimentally to exhibit broken-symmetry structures, including zig-zag chains. Nevertheless, in spite of the large mass of the ions, the superposition (or entanglement) of both the “zig” and “zag” configurations is quantum mechanically allowable, and recently it has been observed experimentally [42].

Even though it is expected that (due to the much smaller electronic mass) the actual CDs of electrons in EQDs and finite length wires would conform to those produced through the symmetry-restoration correction, a promising experimental opportunity emerged recently in the case of 1D domain walls in TMD bilayers [43], where rapid progress in STM imaging could differentiate between symmetry-broken and symmetry-preserving CDs.

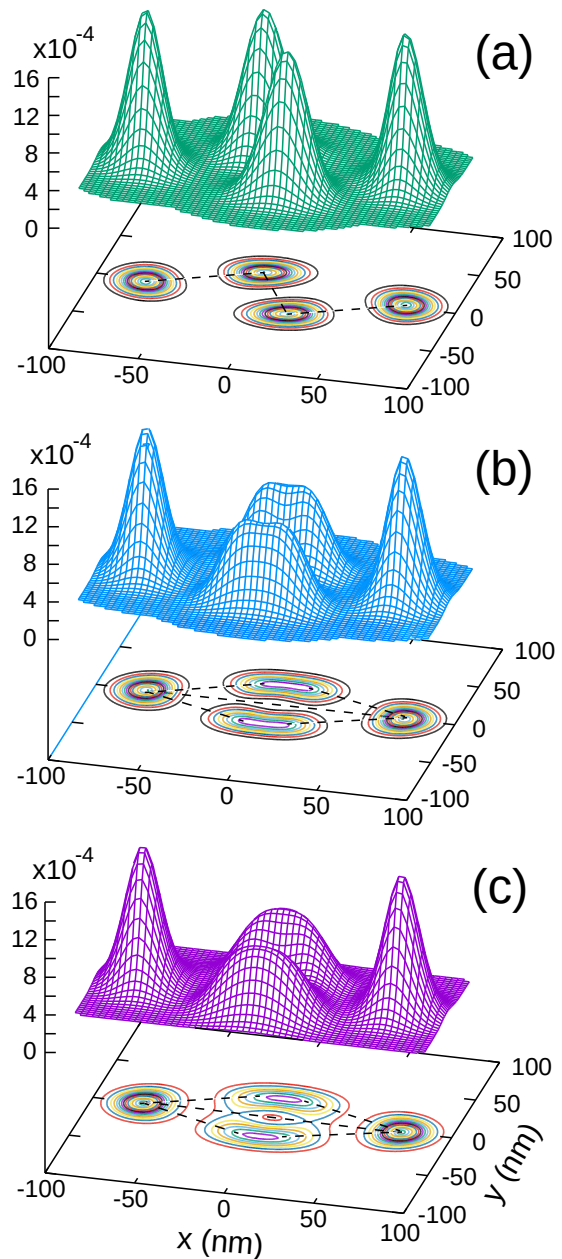


FIG. 7. Comparison of (a) symmetry-broken UHF, (b) y -parity-restored UHF, and (c) FCI CDs for the associated ground states of $N = 4$ electrons at zero magnetic field in a single elliptic quantum dot, with an effective mass $m^* = 0.067m_e$ and a potential confinement specified by $\hbar\omega_x = 3.00$ meV and $\hbar\omega_y = 5.64$ meV. The dielectric constant used was $\kappa = 1$. In (a) and (b), $S_z = 0$. In (c) $S = S_z = 0$. Lengths in units of nm. Charge densities in units of $1/\text{nm}^2$. The charge densities are normalized to the total number of fermions $N = 4$. The dashed lines are a guide to the eye; in (b) and (c), they delineate two mirror trapezoids.

VI. SECOND ENERGY DIFFERENCES

The second difference of the total energies, $\Delta_2 = E(N+1) + E(N-1) - 2E(N)$, corresponding to the

va-UHF electronic configurations shown in Figs. 3 and 4 are shown in Fig. 6. Also shown is the non-interacting case (at maximum occupation per orbital, $\kappa = 300$, and $\hbar\omega_y = 2.5$ meV), which exhibits shell closures at $N = 4, 8, 12$, and 16 according to the Aufbau principle, with the period of 4 resulting from both the spin and valley degrees of freedom. This non-interacting behavior contrasts sharply with that of the strong-interaction cases, where polymeric WM chains are formed. We note that Δ_2 is proportional to the capacitance of the EQD.

VII. AN EXAMPLE OF A COMPARISON WITH FULL CONFIGURATION INTERACTION

In Fig. 7, we present a case of a comparison between UHF and parity-restored UHF charge densities with those from the corresponding FCI [22, 24] calculation. We choose the case of an elliptic external 2D potential that binds $N = 4$ conduction electrons for a one-band (no valley present) semiconductor material.

The UHF CD in Fig. 7(a) displays a broken-symmetry zig-zag configuration. However, restoration of the parity along the y -axis in Fig. 7(b) (which also restores the x -parity in this example) produces a configuration of two mirror trapezoids, which is formed by the spreading out (along the x -axis) of the two middle sharp single-electron humps in panel Fig. 7(a). In this context, note the reduction in height of the corresponding broad humps in Fig. 7(b). The parity-restored UHF CD in Fig. 7(b) is in good agreement with the FCI CD in Fig. 7(c). Naturally, the FCI solution displays a certain degree of additional relaxation effects in the CD humps.

VIII. DISCUSSION AND CONCLUSIONS

We introduced a generalization (referred to as va-UHF) of the unrestricted Hartree-Fock methodology [9, 11, 16, 31] that incorporates the valley degree of freedom on an equal footing with the electronic spin. Furthermore, we explored an augmenting symmetry (here, parity)-restoration step applied to the symmetry-broken va-UHF (going beyond the single determinant description) that amplifies and improves the quantum mechanical description of the considered nanosystem [11, 16, 36]. This new va-UHF methodology is able to effectively and economically investigate the physics of double-quantum-dot-based Si qubits for a number of charge carriers much larger than the number accessible with FCI approaches [14, 16, 22, 24, 29, 30]. The close agreement between the results of charge densities obtained via the symmetry-restored (SR)-UHF methodology and those evaluated by full configuration (exact diagonalization) computations is illustrated in Fig. 7).

A pioneering va-UHF application was presented here for the case of an elongated [7] (referred to also as a jellybean [6]) Si QD. EQDs have been proposed as long-

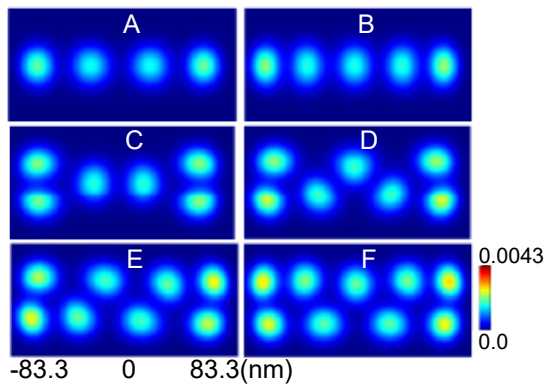


FIG. 8. Ground-state va-UHF charge densities for $N = 4 - 9$ fermions in the same elongated-dot confinement as employed in Fig. 3 of the main text, associated with states with minimum spin and isospin polarizations, as follows: (A) $S_z = 0, V_z = 0, N = 4$. (B) $S_z = 1/2, V_z = 1/2, N = 5$. (C) $S_z = 0, V_z = 0, N = 6$. (D) $S_z = 1/2, V_z = -1/2, N = 7$. (E) $S_z = 0, V_z = 0, N = 8$. (F) $S_z = 1/2, V_z = 1/2, N = 9$. The square-like potential $U_L(x)$ along the x -direction is given by Eq. (1) in the main text with $x_0 = 50$ nm and $\xi = 0.1$ meV. The harmonic confinement $U_T(x)$ along the y -direction has $\hbar\omega_y = 2.5$ meV. Other parameters used: effective mass $m^* = 0.19m_e$ and dielectric constant $\kappa = 11$. Charge densities in units of $1/\text{nm}^2$.

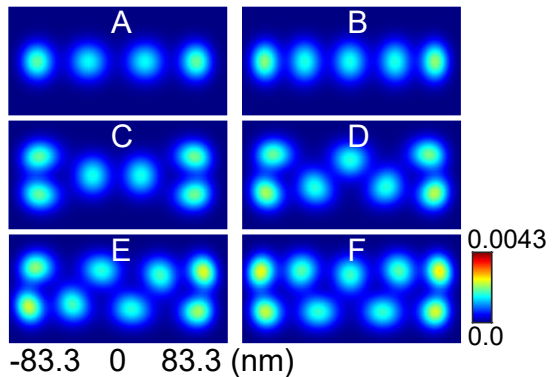


FIG. 9. The fully spin and isospin polarized, ($S_z = V_z = N/2$), va-UHF CDs for $N = 4 - 9$ to be contrasted with those in Fig. 8. Parameters are the same as in the corresponding frames in Fig. 8. CDs in units of $1/\text{nm}^2$.

distance couplers between solid-state qubits, enabling thus an effective solution to the problem of scalability [4–7]. Our calculations for a typical Si EQD revealed a strongly correlated regime as a particular case of Wigner molecularization [9, 11, 16, 17], with the electrons organized in polymeric multi-chain arrangements which are finite-size analogs of the infinite Wigner chains considered earlier [32–35]. In this context, we note that our results agree with the experimental findings of Ref. [7] that the charge is "well distributed" along the long lateral axis of the EQD, whereas Ref. [6] concluded that the electrons bunch together forming several separated QDs.

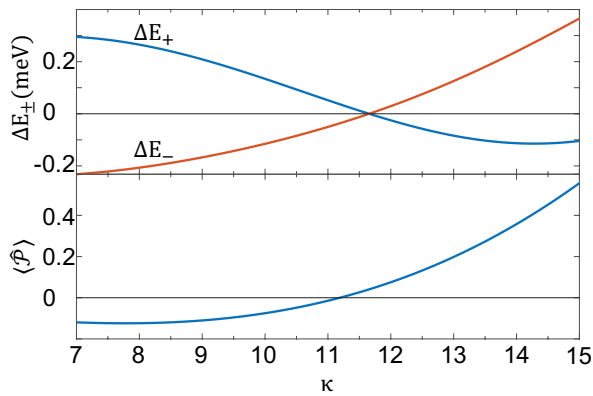


FIG. 10. The energy difference (top), $\Delta E_{\pm} = E_{\text{PUHF}} - E_{\text{UHF}}$ and expectation value of the parity operator (bottom), $\langle \text{UHF} | \mathcal{P} | \text{UHF} \rangle$, for $N = 7$ fully spin and valley polarized electrons as a function of the dielectric constant κ . The \pm subscript corresponds to the two eigenvalues $p = \pm 1$ entering in the definition of the parity projection operator; see Eq. (12) of the main text. The parameters used are: $m^* = 0.19m_e$, $\hbar\omega_y = 2.5$ meV.

Instead of separated QDs, our investigations suggest that the fragmentation in the transverse direction associated with the formation of multiple chains may explain the variety of conductance behaviors reported in Ref. [6]. Conductance calculations between quantum dots coupled to the elongated coupler element, based on the many-body restored-parity va-UHF wave functions, will constitute a promising follow up step of the present paper.

Finally, we note that the va-UHF findings could be further confirmed with a newly developing experimental platform associated with 1D domain walls in twisted TMD bilayers [43].

IX. ACKNOWLEDGMENTS

This work has been supported by a grant from the Air Force Office of Scientific Research (AFOSR) under Grant No. FA9550-21-1-0198. Calculations were carried out at the GATECH Center for Computational Materials Science.

Appendix A: SOME CASES OF CHARGE DENSITIES FOR va-UHF STATES WITH MINIMUM SPIN AND ISOSPIN POLARIZATION

In Fig. 8, we demonstrate that the va-UHF CDs shown in Fig. 3, calculated for the spin and valley fully polar-

ized electrons, are essentially identical to the CDs for the va-UHF states with minimal spin, S_z , and isospin, V_z , projections; see the caption for the specific values. This finding concurs with the magneto-spectroscopy measurements [6] where it has been found that the ‘‘Jellybean’’ quantum dot studied in these experiments lacks visible spin structure for similar electron numbers as those investigated in the present paper. In order to facilitate the direct comparison, we display in Fig. 9 the corresponding fully spin and isospin polarized ($S_z = V_z = N/2$) va-UHF CDs.

Appendix B: AN EXAMPLE OF CALCULATIONS OF PROJECTED ENERGIES

According to Eqs. (12)-(14) of the main text, there are always two projected states, Ψ_{PUHF} , with good parity eigenvalues $p = \pm 1$ for each mixed-parity state, Ψ_{UHF} . The top panel of Fig. 10 demonstrates that one of the symmetry-restored states has always an energy lower (at most equal to) than the broken symmetry UHF state. The bottom panel of Fig. 10 displays the expectation value of the parity operator, $\langle \text{UHF} | \mathcal{P} | \text{UHF} \rangle$, which varies between -1 and +1. Note that, as a function of an increasing dielectric constant κ , the negative-parity projected ground state is replaced by the positive-parity one, following closely a similar behavior by the expectation value.

Appendix C: CLARIFICATION CONCERNING THE COMPACT EXPRESSION IN EQ. (13) OF THE MAIN TEXT

Denoting the va-UHF Slater determinant as $\Psi(x, y)$ (we drop the subscript UHF here), its mirror image about the x axis is given by $\Psi(x, -y)$, and the y -parity restored wave function is $\propto \Psi(x, y) + p\Psi(x, -y)$, with $p = \pm 1$. Then, because the Slater determinant $\Psi(x, -y)$ is in general not orthogonal to $\Psi(x, y)$, the expectation value of an operator \mathcal{O} is given by

$$\frac{\langle \Psi(x, y) | \mathcal{O} | \Psi(x, y) \rangle + p \langle \Psi(x, y) | \mathcal{O} | \Psi(x, -y) \rangle + p \langle \Psi(x, -y) | \mathcal{O} | \Psi(x, y) \rangle + \langle \Psi(x, -y) | \mathcal{O} | \Psi(x, -y) \rangle}{\langle \Psi(x, y) | \Psi(x, y) \rangle + p \langle \Psi(x, y) | \Psi(x, -y) \rangle + p \langle \Psi(x, -y) | \Psi(x, y) \rangle + \langle \Psi(x, -y) | \Psi(x, -y) \rangle}. \quad (\text{C1})$$

The operator associated with the charge density is a one-body operator, $\sum_{i=1}^N \delta(\mathbf{r} - \mathbf{r}_i)$.

-
- [1] F. A. Zwanenburg, A. S. Dzurak, A. Morello, M. Y. Simmons, L. C. L. Hollenberg, G. Klimeck, S. Rogge, S. N. Coppersmith, and M. A. Eriksson, Silicon quantum electronics, *Rev. Mod. Phys.* **85**, 961–1019 (2013).
- [2] A. Warren and S. E. Economou, Silicon qubits move a step closer to achieving error correction, *Nature* **601**, 320–322 (2022).
- [3] G. Burkard, T. D. Ladd, A. Pan, J. M. Nichol, and J. R. Petta, Semiconductor spin qubits, *Rev. Mod. Phys.* **95**, 025003 (2023).
- [4] F. Martins, F. K. Malinowski, P. D. Nissen, S. Fallahi, G. C. Gardner, M. J. Manfra, C. M. Marcus, and F. Kuemmeth, Negative Spin Exchange in a Multielectron Quantum Dot, *Phys. Rev. Lett.* **119**, 227701 (2017).
- [5] F. K. Malinowski, F. Martins, T. B. Smith, S. D. Bartlett, A. C. Doherty, P. D. Nissen, S. Fallahi, G. C. Gardner, M. J. Manfra, C. M. Marcus, and F. Kuemmeth, Spin of a multielectron quantum dot and its interaction with a neighboring electron, *Phys. Rev. X* **8**, 011045 (2018).
- [6] Z. Wang, M. Feng, S. Serrano, W. Gilbert, R. C. C. Leon, T. Tanttu, P. Mai, D. Liang, J. Y. Huang, Y. Su, W. H. Lim, F. E. Hudson, C. C. Escott, A. Morello, C. H. Yang, A. S. Dzurak, A. Saraiva, and A. Laucht, Jellybean quantum dots in silicon for qubit coupling and on-chip quantum chemistry, *Advanced Materials* **35**, 2208557 (2023).
- [7] S. M. Patomäki, J. Williams, F. Berritta, C. Lainé, M. A. Fogarty, R. C. C. Leon, J. Jussot, S. Kubicek, A. Chatterjee, B. Govoreanu, F. Kuemmeth, J. J. L. Morton, and M. F. Gonzalez-Zalba, Elongated quantum dot as a distributed charge sensor, *Phys. Rev. Appl.* **21**, 054042 (2024).
- [8] In the case of a confinement with circular symmetry, the WMs are referred to as rotating WMs as well.
- [9] C. Yannouleas and U. Landman, Spontaneous Symmetry Breaking in Single and Molecular Quantum Dots, *Phys. Rev. Lett.* **82**, 5325–5328 (1999).
- [10] C. Yannouleas and U. Landman, Collective and Independent-Particle Motion in Two-Electron Artificial Atoms, *Phys. Rev. Lett.* **85**, 1726–1729 (2000).
- [11] C. Yannouleas and U. Landman, Strongly correlated wavefunctions for artificial atoms and molecules, *Journal of Physics: Condensed Matter* **14**, L591–L598 (2002).
- [12] A. Harju, S. Siljamäki, and R. M. Nieminen, Wigner molecules in quantum dots: A quantum Monte Carlo study, *Phys. Rev. B* **65**, 075309 (2002).
- [13] S. A. Mikhailov, Two ground-state modifications of quantum-dot beryllium, *Phys. Rev. B* **66**, 153313 (2002).
- [14] C. Yannouleas and U. Landman, Two-dimensional quantum dots in high magnetic fields: Rotating-electron-molecule versus composite-fermion approach, *Phys. Rev. B* **68**, 035326 (2003).
- [15] M. B. Tavernier, E. Anisimovas, F. M. Peeters, B. Szafran, J. Adamowski, and S. Bednarek, Four-electron quantum dot in a magnetic field, *Phys. Rev. B* **68**, 205305 (2003).
- [16] C. Yannouleas and U. Landman, Symmetry breaking and quantum correlations in finite systems: Studies of quantum dots and ultracold Bose gases and related nuclear and chemical methods, *Reports on Progress in Physics* **70**, 2067–2148 (2007).
- [17] C. Yannouleas and U. Landman, Unified microscopic approach to the interplay of pinned-Wigner-solid and liquid behavior of the lowest Landau-level states in the neighborhood of $\nu = 1/3$, *Phys. Rev. B* **84**, 165327 (2011).
- [18] C. Ellenberger, T. Ihn, C. Yannouleas, U. Landman, K. Ensslin, D. Driscoll, and A. C. Gossard, Excitation Spectrum of Two Correlated Electrons in a Lateral Quantum Dot with Negligible Zeeman Splitting, *Phys. Rev. Lett.* **96**, 126806 (2006).
- [19] T. Ihn, C. Ellenberger, K. Ensslin, C. Yannouleas, U. Landman, D. C. Driscoll, and A. C. Gossard, Quantum dots based on parabolic quantum wells: Importance of electronic correlations, *International Journal of Modern Physics B* **21**, 1316–1325 (2007).
- [20] W. Jang, M.-K. Cho, H. Jang, J. Kim, J. Park, G. Kim, B. Kang, H. Jung, V. Umansky, and D. Kim, Single-Shot Readout of a Driven Hybrid Qubit in a GaAs Double Quantum Dot, *Nano Letters* **21**, 4999–5005 (2021).
- [21] C. Yannouleas and U. Landman, Wigner molecules and hybrid qubits, *J. Phys.: Condens. Matter (Letter)* **34**, 21LT01 (2022).
- [22] C. Yannouleas and U. Landman, Molecular formations and spectra due to electron correlations in three-electron hybrid double-well qubits, *Phys. Rev. B* **105**, 205302 (2022).
- [23] J. Corrigan, J. P. Dodson, H. E. Ercan, J. C. Abadillo-Uriel, B. Thorggrimsson, T. J. Knapp, N. Holman, T. McJunkin, S. F. Neyens, E. R. MacQuarrie, R. H. Foote, L. F. Edge, M. Friesen, S. N. Coppersmith, and M. A. Eriksson, Coherent control and spectroscopy of a semiconductor quantum dot Wigner molecule, *Phys. Rev. Lett.* **127**, 127701 (2021).
- [24] C. Yannouleas and U. Landman, Valleytronic full configuration-interaction approach: Application to the excitation spectra of Si double-dot qubits, *Phys. Rev. B* **106**, 195306 (2022).
- [25] S. Pecker, F. Kuemmeth, A. Secchi, M. Rontani, D. C. Ralph, P. L. McEuen, and S. Ilani, Observation and spectroscopy of a two-electron Wigner molecule in an ultraclean carbon nanotube, *Nature Physics* **9**, 576–581 (2013).
- [26] C. Yannouleas and U. Landman, Quantum Wigner molecules in moiré materials, *Phys. Rev. B* **108**, L121411 (2023).
- [27] C. Yannouleas and U. Landman, Wigner-molecule supercrystal in transition metal dichalcogenide moiré superlattices: Lessons from the bottom-up approach, *Phys. Rev. B* **109**, L121302 (2024).
- [28] H. Li, Z. Xiang, A. P. Reddy, T. Devakul, R. Sailus, R. Banerjee, T. Taniguchi, K. Watanabe, S. Tongay, A. Zettl, L. Fu, M. F. Crommie, and F. Wang, Wigner molecular crystals from multi-electron moiré artificial atoms, [arXiv:2312.07607](https://arxiv.org/abs/2312.07607).
- [29] P.-O. Löwdin, Quantum theory of many-particle systems. I. Physical interpretations by means of density matrices, natural spin-orbitals, and convergence problems in the method of configurational interaction, *Phys. Rev.* **97**,

- 1474–1489 (1955).
- [30] I. Shavitt, The history and evolution of configuration interaction, *Molecular Physics* **94**, 3–17 (1998).
- [31] A. Szabo and N. S. Ostlund, *Modern Quantum Chemistry* (McGraw-Hill, New York, 1989).
- [32] G. Piacente, I. V. Schweigert, J. J. Betouras, and F. M. Peeters, Generic properties of a quasi-one-dimensional classical Wigner crystal, *Phys. Rev. B* **69**, 045324 (2004).
- [33] J. S. Meyer and K. A. Matveev, Wigner crystal physics in quantum wires, *Journal of Physics: Condensed Matter* **21**, 023203 (2008).
- [34] S.-C. Ho, H.-J. Chang, C.-H. Chang, S.-T. Lo, G. Creeth, S. Kumar, I. Farrer, D. Ritchie, J. Griffiths, G. Jones, M. Pepper, and T.-M. Chen, Imaging the zigzag Wigner crystal in confinement-tunable quantum wires, *Phys. Rev. Lett.* **121**, 106801 (2018).
- [35] S. Kumar and M. Pepper, Chapter Two - Advances in interaction effects in the quasi one-dimensional electron gas, in *Semiconductor Nanodevices*, Frontiers of Nanoscience, Vol. 20, edited by D. A. Ritchie (Elsevier, 2021) pp. 7–29.
- [36] J. A. Sheikh, J. Dobaczewski, P. Ring, L. M. Robledo, and C. Yannouleas, Symmetry restoration in mean-field approaches, *Journal of Physics G: Nuclear and Particle Physics* **48**, 123001 (2021).
- [37] F. A. Zwanenburg, A. S. Dzurak, A. Morello, M. Y. Simmons, L. C. L. Hollenberg, G. Klimeck, S. Rogge, S. N. Coppersmith, and M. A. Eriksson, Silicon quantum electronics, *Rev. Mod. Phys.* **85**, 961–1019 (2013).
- [38] These confinement-induced single-particle energy states are also referred to as “orbitals”, see, e.g., the expressions “atomic orbitals”, “space orbitals”, and “spin-orbitals” in chemistry [31].
- [39] This is an apparent generalization of the term spin-orbital used in chemistry and molecular physics.
- [40] This behavior contrasts with that in harmonic confinements along the lateral x -direction, where the zig-zag chain starts forming at the center of the linear chain, a fact well known from classical calculations in the literature of trapped heavy ions; see, e.g., Refs. [44–46].
- [41] F. D. Pacati and S. Boffi, Slater determinants, parity projection, and Hartree-Fock calculations, *Phys. Rev. C* **2**, 1205–1210 (1970).
- [42] J. Zhang, B. T. Chow, S. Ejtemaee, and P. C. Haljan, Spectroscopic characterization of the quantum linear-zigzag transition in trapped ions, *npj Quantum Information* **9**, 68 (2023).
- [43] H. Li, Z. Xiang, T. Wang, M. H. Naik, W. Kim, J. Nie, S. Li, Z. Ge, Z. He, Y. Ou, R. Banerjee, T. Taniguchi, K. Watanabe, S. Tongay, A. Zettl, S. G. Louie, M. P. Zaletel, M. F. Crommie, and F. Wang, Imaging tunable Luttinger liquid systems in van der Waals heterostructures (2024), [arXiv:2404.16344](https://arxiv.org/abs/2404.16344) [cond-mat.str-el].
- [44] S. Ejtemaee, *Dynamics of Trapped Ions Near the Linear-Zigzag Structural Phase Transition*, Phd thesis, Simon Fraser University (2015), available at <https://summit.sfu.ca/item/16248>.
- [45] L. L. Yan, W. Wan, L. Chen, F. Zhou, S. J. Gong, X. Tong, and M. Feng, Exploring structural phase transitions of ion crystals, *Scientific Reports* **6**, 21547 (2016).
- [46] J. P. Schiffer, Phase transitions in anisotropically confined ionic crystals, *Phys. Rev. Lett.* **70**, 818–821 (1993).